Geochemistry, Geophysics, Geosystems

RESEARCH ARTICLE
10.1029/2019GC008187

New Constraints on the Thermal Conductivity of the Upper Mantle From Numerical Models of Radiation Transport

Christopher J. Grose[1] **and Juan C. Afonso**[2,3]

[1]Seismological Laboratory, California Institute of Technology, Pasadena, CA, USA, [2]Department of Earth and Planetary Sciences, CCFS/GEMOC, Macquarie University, Sydney, Australia, [3]Now at Centre for Earth Evolution and Dynamics, Department of Geosciences, University of Oslo, Oslo, Norway

Abstract To address uncertainties in the values and mathematical form of the radiative thermal conductivity k_{rad} in the mantle, we developed new models for the transport, scattering, and absorption of thermal radiation in semitransparent multiphase polycrystalline assemblages. We show that the Rosseland diffusion equation correctly describes the diffusion of thermal radiation and infer the form of the effective spectral coefficients through numerical experimentation. We show that the scattering coefficient depends on the grain size and on interphase contact statistics in complicated ways, but that simplifications can be employed in practice. The effective opacity of a composite random material is a harmonically weighted mixture in the limit of infinitely large grain size and an arithmetically weighted mixture in the limit of infinitesimal grain size. Using existing absorption spectra for major upper mantle minerals, we estimate k_{rad} as a function of temperature, grain size, and petrology. In mantle assemblages, the scattering effect is important for small grain sizes (<1 mm), but the grain size effect on the effective opacity of a multiphase medium is important for grain sizes up to 10 cm. We calculate that upper mantle k_{rad} is about 2–3.5 $W{\cdot}m^{-1}{\cdot}K^{-1}$ for a representative mean grain size range of 0.01 to 1 cm. This translates to a total thermal conductivity of 5.5–7 $W{\cdot}m^{-1}{\cdot}K^{-1}$. Application of our model to the cooling of oceanic lithosphere shows that k_{rad} increases net cooling by about 25%.

Key Points:
- Radiative thermal conductivity of ambient upper mantle is estimated to be 2-3.5 W·m−1·K−1; Total thermal conductivity is 5.5-7 W·m−1·K−1
- Radiative thermal conductivity depends strongly on grain size through scattering as well as the effective opacity
- An effective medium theory for radiative thermal conductivity in multiphase polycrystalline assemblages is inferred

Supporting Information:
- Supporting Information S1
- Supporting Information S2

Correspondence to:
C. J. Grose,
chrgrose@mail.usf.edu

Citation:
Grose, C. J., & Afonso, J. C. C. (2019). New constraints on the thermal conductivity of the upper mantle from numerical models of radiation transport. *Geochemistry, Geophysics, Geosystems*, *20*, 2378–2394. https://doi.org/10.1029/2019GC008187

Received 14 JAN 2019
Accepted 7 APR 2019
Accepted article online 13 APR 2019
Published online 22 MAY 2019

1. Introduction

The thermal conductivity k of solid-Earth materials is a fundamental control on the dynamics of planetary interiors across all length and time scales. It is generally recognized that the total thermal conductivity k_{sum} in electronic insulators (e.g., silicate minerals) is the sum of two transport mechanisms: lattice (or phonon) transport and radiative (or photon) transport. A major feature of thermal conductivity is its temperature dependence, which is different for each mechanism. The lattice thermal conductivity k_{lat} typically decreases with temperature, whereas the radiative thermal conductivity k_{rad} increases with temperature (e.g., Hofmeister, 1999). Although knowledge is incomplete for both, k_{lat} is perhaps better understood because lattice transport is fundamentally microscopic and experimental techniques have been developed to reliably isolate lattice transport in single crystals (e.g., Hofmeister et al., 2014). In contrast, direct measurement of radiative thermal conductivity is complicated because the diffusive transport of thermal radiation is a macroscopic phenomenon in semitransparent materials like silicates. The radiative thermal conductivity is thus routinely calculated, not measured, from the spectral properties of minerals (e.g., Schatz & Simmons, 1972) and equations describing diffusive radiation, such as the Rosseland equation (Howell et al., 2011; Rosseland, 1936).

Most previous work on k_{rad} in the Earth has been focused on values in the lower mantle and core-mantle boundary (e.g., Goncharov et al., 2008, 2009, 2015; Keppler et al., 2008; Lobanov et al., 2016). This focus mainly stems from the recognition that lower mantle values control a number of important but poorly understood phenomena such as heat loss of the core (Lay et al., 2008), the generation of the Earth's magnetic field (Stevenson, 2003), and plume formation in the Earth's deep interior (Dubuffet et al., 2002; Matyska & Yuen, 2007; van den Berg et al., 2005). However, experiments have shown that lower mantle minerals are opaque and thus that k_{rad} is low in these settings (e.g., Lobanov et al., 2016, 2017).

Thermal conductivity in the upper mantle is certainly also important. The largest temperature gradients occur in the upper mantle, and heat fluxes down these temperature gradients control the cooling of oceanic lithosphere (e.g., Denlinger, 1992; Grose & Afonso, 2013, 2015; Hasterok, 2013; Parsons & Sclater, 1977; Sclater & Francheteau, 1970), the thermal structure of continental lithosphere (Hasterok & Chapman, 2007, 2011), the reheating of subducting slabs (Maierova et al., 2012; Syracuse et al., 2010), and small-scale convection in the asthenosphere (e.g., Sleep, 2011; Zlotnik et al., 2008). Although spectra of upper mantle minerals at temperature are limited, olivine has been shown to be relatively transparent, suggesting that k_{rad} in the upper mantle is a significant contributor to the total thermal conductivity (Aronson et al., 1970; Clark, 1957; Fukao et al., 1968; Hofmeister, 2005; Schatz & Simmons, 1972; Shankland et al., 1979).

A problem with previous studies is that the use of olivine as a representation of upper mantle material is a nontrivial simplification. The presence and distribution of secondary phases in the mantle assemblage certainly control effective material properties, but it is not clear how. The effective opacity of a composite medium has been addressed in the engineering literature (e.g., Clouet, 1997; Pomraning, 1988; Vanderhaegen, 1988), but no comprehensive theory for polycrystalline media has been offered. Increasing confusion still further, some aspects of the fundamental equations have recently been disputed (Hofmeister, 2014).

In this work, we attempt to clarify the nature of radiative heat transport in mantle assemblages using numerical techniques which treat the fundamental behavior of thermal radiation. We first set the stage for an analysis of mantle k_{rad} with an overview of k_{rad} fundamentals and some previous efforts to constrain mantle k_{rad}. Next, we describe our approach of using digital microstructures representing multiphase polycrystalline rocks and simulating radiation transport within these microstructures with new models for the diffusion of thermal radiation. By studying radiation transport in synthetic assemblages with widely varied spectral properties, we confirm that the Rosseland diffusion equation describes k_{rad} and develop a general effective medium theory for the mean free path. We use our models to estimate mantle k_{rad} as a function of temperature, grain size, and mineralogy. As an application of our theory we calculate k_{rad} for a petrologically realistic upper mantle assemblage as a function of temperature, depth, and grain size. We also consider the classical problem of cooling oceanic lithosphere using our final model.

2. k_{rad} Overview

All materials at finite temperature emit thermal radiation. In a semitransparent medium, emitted radiation is transported a distance away from its origin. During transport, radiation is gradually absorbed by the medium and scatters as it encounters defects and boundaries. For an isolated system in which all parts have equal temperature, the system will be in thermodynamic and radiative equilibrium. The intensity of locally emitted and absorbed radiation is everywhere equal, resulting in no change in temperature over time. However, if a temperature gradient exists, the region of higher temperature will emit more energy than it receives and a net flux of thermal radiation occurs until thermodynamic equilibrium is achieved. When the distance over which a temperature gradient exists is large compared to the mean free path of radiation, the medium is said to be optically thick and heat flux down the gradient is a diffusive process. The flux of heat in such a system is described by the Rosseland diffusion equation (Howell et al., 2011; Rosseland, 1936)

$$q_{r,x} = -\frac{4\pi}{3}\int_0^\infty l_\nu \frac{\partial n_\nu^2 I_{\nu b}}{\partial x} d\nu, \tag{1}$$

where x is distance in the direction of the flux vector, $I_{\nu b}$ is the black body radiance per unit frequency ν and per unit solid angle given by the Planck function

$$I_{\nu b}(\nu, T) = \frac{2h\nu^3}{c^2}\left[\exp\left(\frac{h\nu}{k_b T}\right) - 1\right]^{-1}, \tag{2}$$

where h is the Planck constant, c is the speed of light in a vacuum, k_b is the Boltzmann constant, T is temperature, and where l_ν is the spectral mean free path composed as

$$l_\nu = \frac{1}{e_\nu} = \frac{1}{A_\nu + \sigma_\nu}, \tag{3}$$

where e_ν, A_ν, and σ_ν are the spectral extinction, absorption, and scattering coefficients, respectively. As materials with high A are opaque to radiation, A is also referred to as the opacity. From Fourier's law, the associated radiative thermal conductivity is therefore

$$k_{rad} = -q_{r,x}\left(\frac{\partial T}{\partial x}\right)^{-1} = \frac{4\pi}{3}\int_0^\infty l_\nu \frac{\partial n_\nu^2 I_{\nu b}}{\partial T} d\nu. \quad (4)$$

For a homogeneous single-phase medium with known absorption spectra and no scattering, the calculation of radiative thermal conductivity is straightforward from equation (4) (Clark, 1957; Goncharov et al., 2015; Keppler et al., 2008; Shankland et al., 1979). However, for a material with highly transparent spectral bands, multiple phases, and small grain size, the process of scattering may be significant and the effective spectral coefficients are not straightforward to define. Previously, the role of scattering in solid-Earth materials has usually been ignored due to poor constraints, simplicity, or the assumption that it is negligible (Aronson et al., 1970; Clark, 1957; Hofmeister, 1999; Shankland et al., 1979). Shärmeli (1979) attempted to experimentally constrain the scattering coefficient in a typical olivine polycrystal based on an assumed functional form of the temperature-dependent lattice conductivity, but no fundamental theory was offered. Clark (1957) recognized that the scattering coefficient must be proportional to ϵ/d where d is the grain diameter and ϵ is a factor related to the grain boundary reflection coefficient, averaged over all angles of incidence, and is less than unity. Similarly, Pitt and Tozer (1970) and Nitsan (1976) argued that this form is correct and that the value of ϵ is of the order 0.02. We will later conclude with a formulation in some agreement with this view. However, Hofmeister (2005) and Hofmeister and Yuen (2007) recently developed a k_{rad} model with particularly unique characteristics. Their formulation predicts that as the grain size or A_ν goes to either zero or infinity, k_{rad} goes to 0. This agrees with equations (3)–(4) for the case where e_ν goes to ∞ but not for cases where e_ν goes to 0 since the mean free path and heat flux should become infinite.

If the medium consists of multiple phases characterized by unique refractive indices and absorption spectra, then A_ν must have some effective value for the mixture. The effective opacity in random media has been a subject of some work in the engineering literature (e.g., Clouet, 1997; Pomraning, 1988; Vanderhaegen, 1988), although investigations have usually been confined to two-phase media in which second phases are spherical. Including all effects together in multiphase polycrystalline media results in a complicated problem for which a general effective medium theory is so far unavailable. Moreover, Hofmeister (2014) has suggested that the usual inclusion of n^2 in the source function $n^2 I_{\nu b}$ (equation (4)) is fundamentally erroneous, although we dispute this (supporting information section S1).

3. Methods

3.1. Microstructure Model

Our modeling strategy is twofold. First, we generate digital microstructures which accurately characterize the geometry of crystals and the distribution of phases in 3-D space. For this we employ the Monte-Carlo Potts model (c.f., Janssens et al., 2007; Tikare et al., 1998), which is a dimensionless, albeit time-dependent statistical thermodynamics model frequently used to represent material coarsening processes. We developed a model adapted for multiple phases and high surface resolution. For our experiments we generate 2-D and 3-D micsotructures with, on the order of, 100 grains with arbitrarily defined phase fractions. In the case of representative mantle assemblages, we use phase fractions from equilibrium thermodynamic calculations (Connolly, 2009; Xu et al., 2008) for the composition of fertile mantle peridotite (Herzberg, 2004). A typical mantle microstructure is shown in Figure 1. Details are provided in supporting information section S2.

3.2. Radiation Transport Modeling

The second part of our modeling strategy is to use the method of Monte-Carlo radiation transport to describe radiation transport in synthetic microstructures. In Monte-Carlo radiation transport, photons (or "photon bundles") are emitted and transmitted through a medium and interact with it by scattering off grain boundaries according to the Snell and Fresnel equations and gradually lose energy to the medium until all energy is absorbed. The general feature of models which allow calculation of k_{rad} is the gradual absorption of radiation with distance from its emission site.

To study the diffusion of thermal radiation in materials we designed two model applications of the Monte-Carlo radiation transport method. In both of these models, a large number of photons are emitted in all directions at all radiant frequencies from all parts of the microstructure. The first model is a formulation which we call Ballistic Radiation Transport in which radiation emission and transport is modeled explicitly in space according to the time-dependent temperature field and spectral heterogeneity of the medium, and

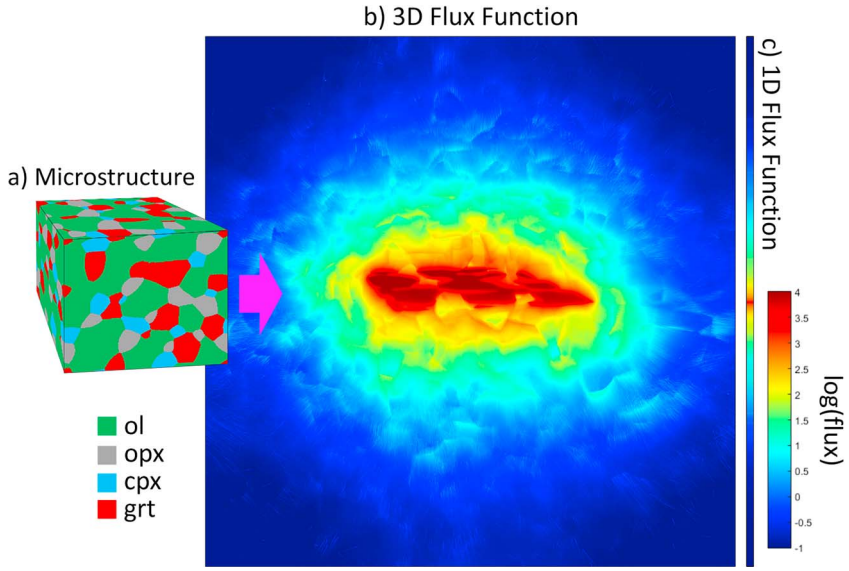

Figure 1. Illustration showing (a) an example 3-D microstructure representing the upper mantle assemblage, and flux functions for absorbed radiative energy in (b) 3-D, and (c) 1-D. The 3-D flux function shows a perspective view for all emissions originating from a plane in the microstructure. Notice that the plane from which emission originates in this illustration corresponds with the top surface of the microstructure shown in (a). Also, note that we take the log of the flux for the purposes of visualization only. ol = olivine; opx = orthopyroxene; cpx = clinopyroxene; grt = garnet.

k_{rad} is estimated from the resulting thermal evolution. The essence of the method is the use of Monte-Carlo transport to construct functions for the absorbed and emitted energy such that thermal evolution is described by solving an equation of the form

$$C_v \frac{\partial T}{\partial t} = \int_0^\infty (Q_r - E_r) d\nu, \tag{5}$$

where C_v is isobaric heat capacity, t is time, Q_r is a function for radiative energy absorbed, and E_r is a function for radiative energy emitted. Although the emission function is straightforward, the absorption function depends on the transport of photons throughout the microstructure. Figure 1 shows a perspective view of such a function in the case that the emitting plane is hot and the surroundings are zero temperature (none-mitting). Because the phase distribution results in optical heterogeneity it is easy to perceive the opaque phases as incident radiation is more strongly absorbed when traversing them. The second model approach is a simplification of the first which we call Diffusive Radiation Transport. In this approach, Monte-Carlo techniques are used to estimate the mean free path of radiation from a large sample of rays emitted throughout the polycrystal. After the mean free path is obtained from Diffusive Radiation Transport, k_{rad} can be calculated via equation (4). Details of the Monte-Carlo radiation transport approach are provided in supporting information section S3 and the Ballistic Radiation Transport and Diffusive Radiation Transport methods are developed in supporting information section S4.

4. Effective Medium Theory

From sensitivity analysis of Diffusive Radiation Transport models in microstructures generated by the Monte-Carlo Potts model, we have developed a comprehensive homogenization, or effective medium theory, for the mean free path of radiation in isotropic multiphase polycrystalline assemblages. Figure 2a shows predictions of k_{rad} from 3-D Diffusive Radiation Transport models in single-phase defect-free mediums with $A_\nu = 2$ cm^{-1} over all frequencies, $T = 500$ K, and a constant refractive index between 1 and 3. Since the refractive index is everywhere constant in these tests, scattering does not occur, but k_{rad} increases due to a dependence on n^2 (supporting information section S1). Our radiation transport calculations and the Rosseland diffusion equation are consistent, confirming that the Rosseland equation is at least correct for homogeneous media. The remaining question is thus whether or not the Rosseland equation can be applied to an inhomogeneous medium, which requires that there be an effective mean free path which can be represented in terms of effective spectral coefficients ($n_{e,\nu}$, $A_{e,\nu}$, and $\sigma_{e,\nu}$).

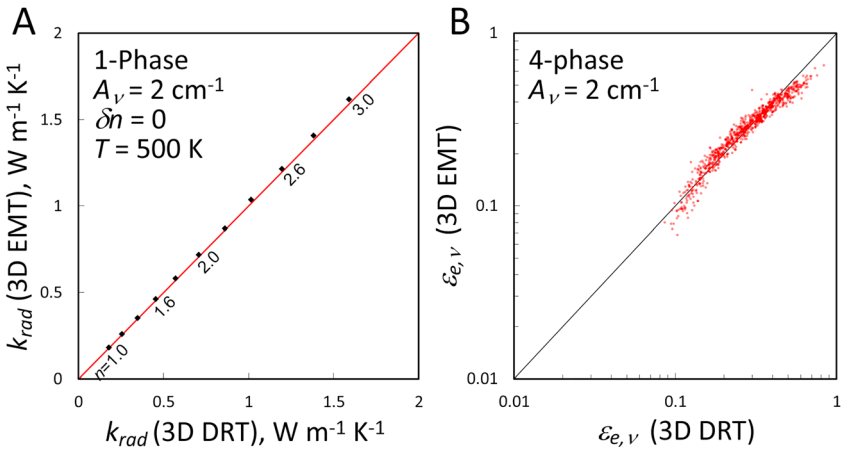

Figure 2. (a) Predictions of k_{rad} for semi-infinite (single-phase) crystals from 3-D Diffusive Radiation Transport (DRT) versus that predicted from the Rosseland diffusion equation (equation (4)). (b) Comparison of scattering interaction parameters predicted by our Diffusive Radiation Transport models and our effective medium theory (EMT).

4.1. Effective Spectral Coefficients

The effective refractive index of a multiphase polycrystal was found to be arithmetically weighted as

$$n_{e,\nu}^2 = \frac{1}{V}\int_V n_\nu^2 dV = \sum_k^{N_k} \phi_k n_{k,\nu}^2, \tag{6}$$

where ϕ_k is the volume fraction of phase k and N_k is the number of phases in the medium. The mixing law describing the effective opacity A_e is substantially more complicated because of a dependence on grain size as well as phase fractions. Figure 3 shows calculations of A_e as a function of mean grain size r_m for a two-phase assemblage with equal phase fractions, a homogeneous refractive index, and where one phase is defined by $A = 2$ cm^{-1} and the other phase is defined by A between 10 and 100 cm^{-1}. 3-D Diffusive Radiation Transport

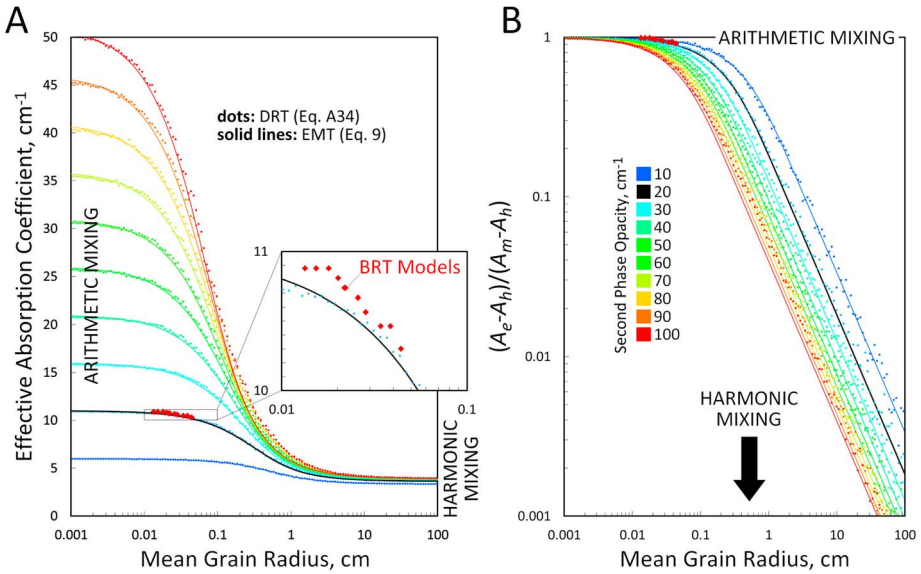

Figure 3. (a) Calculations of the effective absorption coefficient A_e (opacity) of a two-phase composite medium with equal phase fractions over a large grain-size range and where the first phase has the opacity of 2 cm^{-1} and the second phase opacity is between 10 and 100 cm^{-1}. Dots show predictions from individual Diffusive Radiation Transport (DRT) models (see supporting information section S4) and solid lines show predictions of our effective medium theory (EMT) from equation (14). The black line highlights the case where the second phase has the opacity of 20 cm^{-1}. The red diamonds show predictions of our ballistic radiation transport (BRT) models which have the same optical properties as the model indicated by the black line. The inset figure shows a close-up of the Ballistic Radiation Transport calculation results. (b) The same model predictions relative to the arithmetic upper limit A_m and harmonic lower limit A_h.

predictions are shown as dots and the solid lines are predictions of an analytic model inferred from the former (discussed below). Each dot represents a calculation for a unique randomly generated microstructure, resulting in some noise. The results indicate that in the limit of infinitely large grain size the opacity mixing law is harmonic

$$\frac{1}{A_{e,\nu}} = \frac{1}{A_{h,\nu}} = \frac{1}{V}\int_V \frac{dV}{A_\nu} = \sum_k^{N_k} \frac{\phi_k}{A_{k,\nu}}, \tag{7}$$

whereas in the limit of infinitely small grain size the mixing law is arithmetic

$$A_{e,\nu} = A_{m,\nu} = \frac{1}{V}\int_V A_\nu dV = \sum_k^{N_k} \phi_k A_{k,\nu}. \tag{8}$$

These bounds likely originate in the fact that rays traveling through fine grained media will sample many crystals of different phases before extinction, resulting in an average of the phases, whereas a ray traveling through coarse grained media will mainly sample the phase it is emitted from, so bulk transport is dominated by transparent phases. Critically, the grain size range over which A_e varies substantially occurs over many orders of magnitude. Moreover, the grain size range where A_e varies is well within the likely mantle grain size range. Thus, the grain size effect on the opacity is critical for estimating mantle k_{rad}, as has been recognized in the engineering literature (e.g., Clouet, 1997; Pomraning, 1988; Vanderhaegen, 1988). Although the Diffusive Radiation Transport method provides a low level constraint on effective optical properties, a simpler analytic function is desirable for practical applications. Although we did not derive a physical theory, through inspection we found that the following approximation closely fits the Diffusive Radiation Transport results:

$$A_{e,\nu} = \frac{b}{r_m}\left[1 - \exp\left(-\frac{r_m}{b}\right)\right]\left(A_{m,\nu} - A_{h,\nu}\right) + A_{h,\nu}, \tag{9}$$

where

$$r_m = \frac{1}{V}\int_V r_V dV \tag{10}$$

is the grain size where r_V is the radius of the crystal occupied by the volume dV, and

$$b = \frac{2}{A_m} = 2 - \frac{1}{2}A_h. \tag{11}$$

Predictions of this mixing law are given as solid lines in Figure 3. There is some underestimation of A_e from the law when grain size is about 0.1–1 cm and the opacity contrast is large. This remains true in our calculations for mantle assemblages as spectral bands with high opacity contrast give different results by Diffusive Radiation Transport and equation (9). In our view the most likely problem is that our Diffusive Radiation Transport models become inaccurate representations of random media when the opacity contrast is large because our microstructures do not contain enough grains. Our effective medium theory with the above mixing law is thus preferred.

Equation (9) shows that the grain size at which there is a transition between arithmetic and harmonic mixing regimes is determined by the product of the grain size and the mean opacity. For example, if we define a transition grain size r_t as the size at which $A_e = wA_m + (1 - w)A_h$, r_t may be found by solving

$$\frac{2}{r_t A_m}\left[1 - \exp\left(-\frac{r_t A_m}{2}\right)\right] = w. \tag{12}$$

In the case where $w = 0.5$, the solution is simply

$$r_t = \frac{3.18725}{A_m}. \tag{13}$$

Thus, increasing the mean opacity by some factor will decrease the transition size by the same factor. This also implies that the transition size is linearly proportional to the mean free path.

4.2. Geometric Scattering

The effective scattering coefficient is complex due to a dependence on grain size as well as phase distribution. We studied the magnitude of the scattering parameter by constructing digital microstructures with a constant absorption coefficient and assigning a random refractive index for each crystal according to its phase and orientation. In all cases we assumed that the refractive index was isotropic. Although effective opacity calculations may use a simplified form of Diffusive Radiation Transport calculation, based on renewal theory (see supporting information section S5), we use full 3-D calculations without simplifications to account for the geometric complexity of scattering effects. We calculated $\sigma_{e,\nu}$ as

$$\sigma_{e,\nu} = e_{e,\nu} - A_{e,\nu} \tag{14}$$

from 10^3 Diffusive Radiation Transport simulations each with randomly generated four-phase microstructures with random phase fractions, $A_\nu = 2\,\mathrm{cm}^{-1}$ everywhere, and a random refractive index for each crystal generated as $n_c = a_k + b_{k,c}$, where a_k is a random number between 1 and 3 for each phase k, and $b_{k,c}$ is a random number between 0 and 1 for each crystal c of phase k.

Consistent with Clark (1957), results of our 3-D Diffusive Radiation Transport models suggest that scattering in isotropic equilibrium microstructures with isotropic spectral coefficients is described by

$$\sigma_{e,\nu} = \frac{\varepsilon_{e,\nu}}{r_m}, \tag{15}$$

where $\varepsilon_{e,\nu}$ is a dimensionless coefficient describing the scattering interaction. We find that a form for $\varepsilon_{e,\nu}$ which closely fits the 3-D Diffusive Radiation Transport results is

$$\varepsilon_{e,\nu} = \frac{\delta n_{e,\nu}}{n_{e,\nu}}, \tag{16}$$

where

$$n_{e,\nu} = \frac{1}{V}\int_V n_\nu dV \tag{17}$$

is the mean refractive index of the medium and

$$\delta n_{e,\nu} = \frac{1}{\hat{S}}\int_0^\infty \Delta n_{\nu,S} S(\Delta n_{\nu,S} < n_i) dn_i \tag{18}$$

is the mean n mismatch (Δn_ν) along all grain surface areas S in the volume, where $\hat{S}$ is the total grain boundary surface area, $S(\Delta n_{\nu,S} < n_i)$ is surface area where $\delta n_{\nu,S} < n_i$ and n_i is refractive index over which to integrate. Equation (18) may also be rewritten in terms of grain contact statistics as

$$\delta n_{e,\nu} = \sum_k^{N_k}\sum_{\ell\le k}^{N_k} \delta\hat{n}_{k\ell} f_{k\ell}, \tag{19}$$

where N_k is the number of phases, $f_{k\ell}$ is the surface area fraction of contacts between phase k and ℓ given by

$$f_{k\ell} = \frac{1}{\hat{S}}\int_S g_{k\ell} ds, \tag{20}$$

where

$$g_{k\ell} = \begin{cases} 1 & s \in \delta\Omega_k \cap \delta\Omega_\ell \\ 0 & s \notin \delta\Omega_k \cap \delta\Omega_\ell \end{cases} \tag{21}$$

is the discontinuous function defining the surface area where phase k and ℓ are in contact, $\delta\Omega_k$ is the surface of domains of phase k, and where $\delta\hat{n}_{k\ell}$ is the mean refractive index mismatch between phase k and ℓ given as

$$\delta\hat{n}_{k\ell} = \frac{\int_0^\infty\int_0^\infty P_k P_\ell |n_k - n_\ell| dn_k dn_\ell}{\int_0^\infty\int_0^\infty P_k P_\ell dn_k dn_\ell}, \tag{22}$$

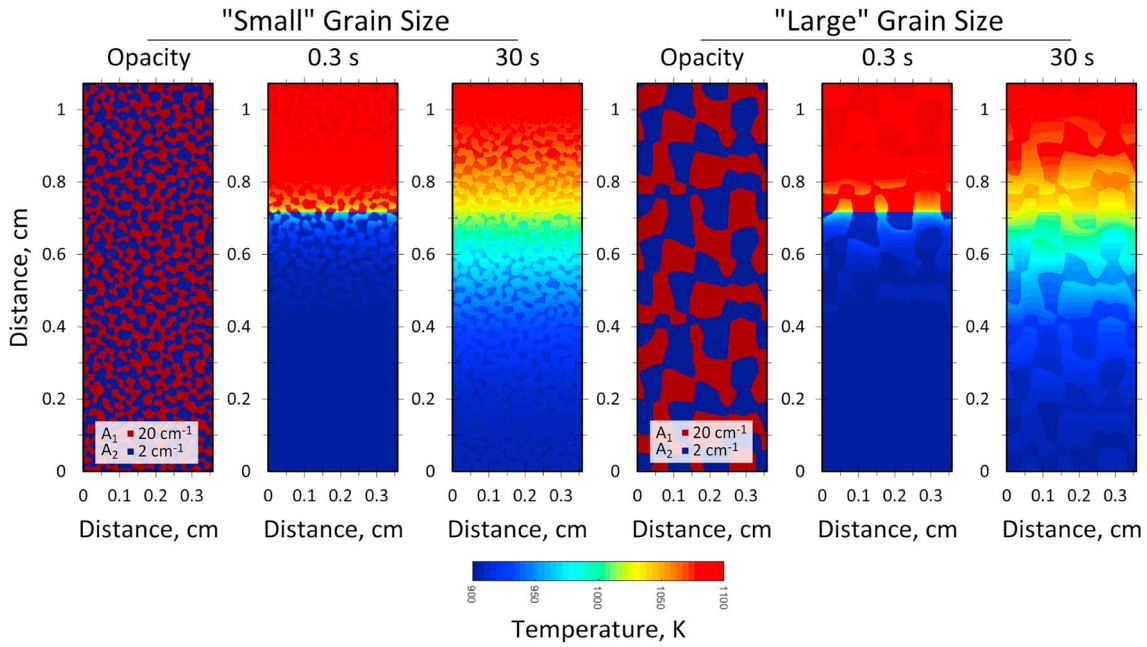

Figure 4. The 2-D Ballistic Radiation Transport simulations of the cooling of a warm block in a fine (left three panels) and coarse grained (right three panels) medium. For each model the panels show the spectral heterogeneity, temperature after the first time step (0.3 s), and after 100 time steps (30 s). In the full models the boundary conditions are everywhere periodic, but only the bottom half of the model results are shown (further explanation in text and in the supporting information). Effective opacities for these models (and intermediate grain sizes) are shown as red diamonds in Figure3.

where n_k and n_ℓ are refractive indices in phases k and ℓ, respectively, and P_k and P_ℓ are density functions for the refractive indices in phases k and ℓ, respectively. Although we have developed methods for obtaining contact statistics from arbitrarily complicated digital microstructures, we have not obtained expressions which independently characterize the statistics for more than two phases (supporting information section S7).

Figure 2b shows the consistency between $\varepsilon_{e,v}$ calculated from the above effective medium theory (equations (15)–(18)) versus that from 3-D Diffusive Radiation Transport simulations. Although agreement is good, the effective medium calculation underpredicts $\varepsilon_{e,v}$ for large and small values. Underprediction of low values probably originates from a numerical error in the value of $A_{e,v}$ which becomes pronounced as the computation of $\sigma_{e,v}$ from equation (14) approaches a small but erroneous residual (since $A_{e,v}$ is known a priori, while $e_{e,v}$ is approximated by the model) as scattering decreases, and not the correct value of zero. On the other hand, underprediction of high effective medium values probably originates from low resolution of our voxel mesh and surface normal vectors which become noticeable when photons interact with surfaces where the refractive index mismatch is large (which are required for large values of this coefficient). As the refractive index mismatch increases, the reflectivity and transmission angles for rays incident on high refractive index crystals increase. Correctly describing geometric scattering with such extreme values likely requires a more accurate description of the topology of microstructures which exceeds the limits of our numerical techniques (supporting information section S2). Alternatively, our homogenization for $\sigma_{e,v}$ may only be an approximation. In either case our approximation is reasonable for mantle physics as refractive indices in real materials are much more restrictive than in our tests.

5. Ballistic and Grain-Scale Effects

So far our analysis has shown that the Rosseland diffusion equation is essentially correct in optically thick conditions. k_{rad} is proportional to the integrated product of the spectral mean free path and the temperature derivative of the source function (equation (4)). However, consider that in an optically heterogeneous medium the temperature gradient will not be exactly linear at the grain-scale. Optical heterogeneity, at least in the case of large grain size, should result in smaller temperature gradients in transparent phases compared to opaque phases, which may result in a complicated deviation from the predictions of the Rosseland

equation with effective mean free path. Using ballistic radiation transport models, we constructed numerical experiments in an attempt to measure such an effect.

We calculated A_e from eleven 2-D Ballistic Radiation Transport models with grain sizes between 0.013 and 0.044 cm and show results in Figure 3 so that they may be compared to previously discussed Diffusive Radiation Transport and effective medium calculations. Each Ballistic Radiation Transport model has two phases with equal phase fractions, with $A = 2$ cm^{-1} for the first phase and $A = 20$ cm^{-1} for the second phase. The model is an elongate 6x tessellated periodic microstructure initially at 900 K with a central block at 1100 K. Boundary conditions are periodic. Figure 4 shows the temperature field for the two Ballistic Radiation Transport models with the smallest and largest grain size after 0.3 (one time step) and 30 s (100 time steps) of heat transport. The cooling of the hot region occurs by radiation transport, and we only show cooling of one side of the model to save space, since the other side is nearly a reflection. In these models, k_{rad} calculated from the effective cooling rate is initially variable (ballistic behavior in the optically thin regime) but approaches a constant value after a few hundred seconds (see Figure S1), showing that heat transport evolves from a ballistic to a diffusive process as temperature gradients relax. When transport is diffusive, A_e is computed from k_{rad} and taken to represent an optically thick medium. Calculated A_e closely follows the effective medium prediction, within a few percent error (see closeup in Figure 3a). Although the calculations are consistent, we were not able to fully confirm the grain size effect predicted by our effective medium theory (i.e., harmonic mixing at large grain sizes) because numerical tests of our Ballistic Radiation Transport techniques showed that large grain size models (or models with more opaque phases) become contaminated by inaccuracies that cannot be resolved unless larger computational resources are employed. In the future, we will improve our techniques so that reduced computational requirements increase the tractability of Ballistic Radiation Transport models with large grain sizes.

In additional tests, we were able to show that k_{rad} and k_{lat} mechanisms are coupled via the temperature field (supporting information section S6). For example, the effective thermal conductivity of a random grainy medium can be described by a geometric mixing law (e.g., Abdulagatova et al., 2009; Fuchs et al., 2013)

$$k_{e,lat} \approx \prod_{k}^{N_k} k_{k,lat}^{\phi_k}, \tag{23}$$

where $k_{k,lat}$ is the lattice thermal conductivity of phase k and ϕ_k is the volume fraction of phase k. However, we solved the coupled conduction-radiation equation

$$C_v \frac{\partial T}{\partial t} = \nabla \cdot k_{lat} \nabla T + \int_0^\infty (Q_r - E_r) d\nu, \tag{24}$$

in microstructures like those in Figure 4. It is typically assumed that the total thermal conductivity is the sum of the transport mechanisms

$$k_{e,sum} = k_{e,lat} + k_{rad}. \tag{25}$$

Although this is surely the case in principle, it is not necessarily the case that the values of each transport mechanism are independent of the other. Our tests showed that when k_{lat} of one phase is much lower than the other, it acts as a bottleneck to transport, as expected from equation (23). However, if the low k_{lat} phase is also transparent, heat is transmitted by radiation, perturbing the temperature field. The result is that the bottlenecking effect is reduced and the geometric law underpredicts $k_{e,lat}$. Fortunately, our tests also showed that the coupling effect is only important for extreme conductivity and opacity contrasts and so may only be relevant for porous media in which one phase is a gas. Equation (27) can thus be reasonably applied to solid-Earth heat transport problems, with values of each mechanism independently constrained (e.g., equation (4) for k_{rad} and equation (23) for $k_{e,lat}$). Details for these tests are provided in supporting information section S6.

6. Predictions of k_{rad} in the Upper Mantle

6.1. Absorption Spectra

k_{rad} prediction in the mantle assemblage requires empirical data for the spectral coefficients (n_ν and A_ν) as a function of temperature, pressure, and phase. Absorption spectra of $Mg_{0.9}Fe_{0.1}SiO_4$ olivine has been described by Hofmeister (2005) that based on her measurements and low-temperature

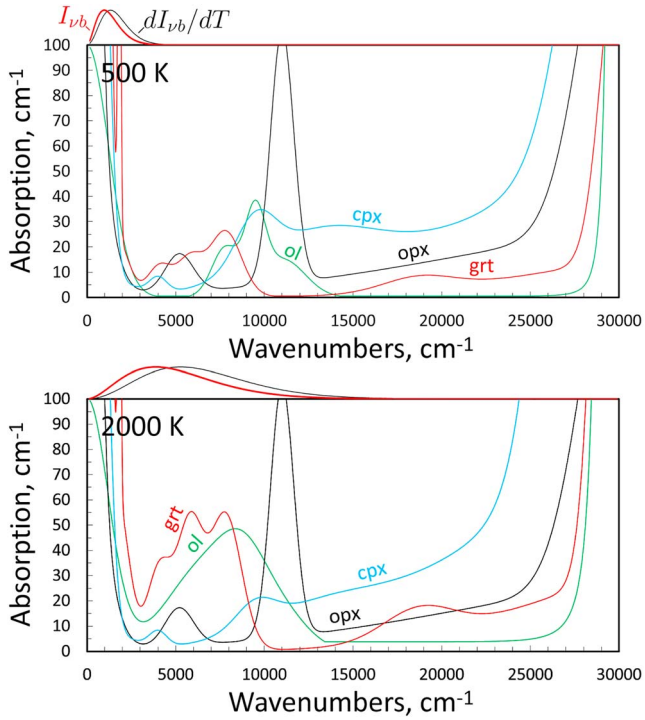

Figure 5. Fitted functions to absorption spectra for the upper mantle phases olivine (ol), orthopyroxene (opx), clinopyroxene (cpx), and garnet (grt) at 500 (top) and 2000 K (bottom). Also shown at the top of each panel is the planck function $I_{\nu b}$ and its temperature derivative (the horizontal scale is as given, but only relative values on the vertical scale are important). See text for data sources.

spectra from Taran and Langer (2001) and high-temperature from Ullrich et al. (2002). We also use low-temperature spectra from Taran and Langer (2001) and Taran et al. (2007) for $(Mg_{1.63}Fe_{0.27}Ca_{0.04}Al_{0.02})^{[6]}Si_{1.97}Al_{0.03}O_6$ clinopyroxene, $(Ca_{0.84}Na_{0.12}Fe_{0.01})^{[8]}(Mg_{0.91}Fe_{0.07}Cr_{0.02})^{[6]}Si_{2.03}O_6$ orthopyroxene, and $(Mg_{1.282}Fe_{1.312}Mn_{0.028}Ca_{0.413})^{[8]}(Fe_{0.04}Al_{1.97}Si_{2.971})^{[6]}O_{12}$ garnet. For pyroxene spectra we approximate the average of crystallographic orientations. Temperature-dependence of absorption spectra for these phases is estimated by linear extrapolation, for each frequency, from measurements within a range of low-temperatures (300–600 K). This is an unsatisfying extrapolation, but if no extrapolation were made to estimate temperature dependence, predicted k_{rad} would be significantly higher. Future measurements at high temperature will be needed to corroborate or correct these spectra. Figure 5 shows absorption spectra for each phase used in our calculations at 500 and 2000 K. Note that the Planck function and its temperature derivative are also shown.

For refractive indices, and their variation, we assume equal distributions about a mean value for each phase. In our models, the refractive index is 1.64 ± 0.045 for olivine, 1.66 ± 0.045 for orthopyroxene, 1.69 ± 0.045 for clinopyroxene, and 1.73 ± 0.03 for garnet. Ranges represent the variation due to anisotropy and composition. Because garnet is optically isotropic, it has a smaller range. Values for olivine are based on Laskowski and Scotford (1980), pyroxenes are based on Deer et al. (1997), and garnet is based on Sriramadas (1957). In our model, each individual grain in the microstructure has a single randomly defined characteristic refractive index which is within the prescribed range for its phase.

6.2. k_{rad} in Single-Phase Polycrystals

Figure 6a illustrates predictions of k_{rad} using our effective medium theory for olivine polycrystals in the grain size range between 0.01 and 1 cm. Our predictions for orthopyroxene, clinopyroxene, garnet polycrystals, and the upper mantle assemblage (UM) are also shown, although we only highlight the range of their estimates within the same grain size range to reduce clutter (see Figure S2 for more information). Our results are also compared to estimates for olivine from previous authors (Fukao et al., 1968; Schatz & Simmons, 1972; Shankland et al., 1979). The general agreement with these previous reports can be attributed to a common physics via the Rosseland diffusion equation (equations (1)–(4)), as well as similar olivine spec-

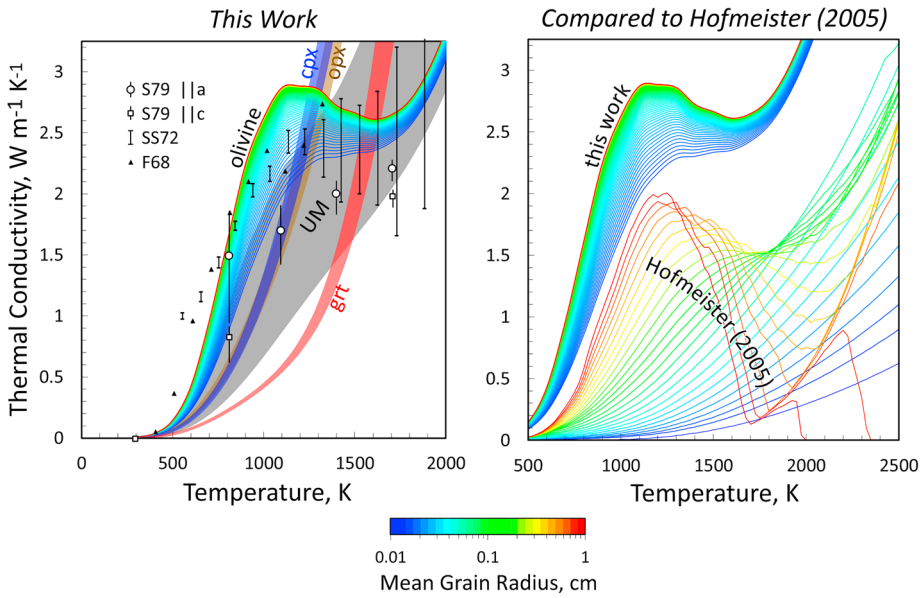

Figure 6. (a) Olivine k_{rad} as a function of temperature and grain size predicted by our models compared to previous estimates by Fukao et al. (1968), Schatz and Simmons (1972), and Shankland et al. (1979), or F68, SS72, and S79, respectively. Also shown are predictions of single-phase models for cpx, opx, grt, and UM. For olivine we show curves for a range of grain sizes with each grain size having its own curve. Predictions for opx, cpx, and garnet are also shown for the same grain size range but the estimated ranges are merely highlighted to reduce clutter. (b) Our predictions of olivine compared to the model for mantle olivine from Hofmeister (2005). cpx = clinopyroxene; opx = orthopyroxene; grt = garnet; UM = upper mantle.

tra. Our predictions for olivine provide a reasonably close fit to previous estimates by Schatz and Simmons (1972) and Fukao et al. (1968) for $T > 800$ K. Olivine is transparent to thermal radiation at low temperature, but becomes more opaque than pyroxenes around 1200 K and more opaque than garnet around 1500 K. Orthopyroxene and clinopyroxene have similar k_{rad} over all temperatures. Garnet is the most opaque at low temperature. Notice how the scattering effect does not affect k_{rad} unless grain size is less than about 1 mm. In contrast, Figure 6b compares our olivine predictions to the olivine model of Hofmeister (2005). Because absorption spectra are the same in both models, the differences reflect major deviations in theory. Overall, Hofmeister (2005) model predicts a significantly larger dependence on grain size, overall lower k_{rad}, and zero k_{rad} for high temperatures and large grain size. The prediction that k_{rad} goes to zero at high temperature for large grain sizes in the model of Hofmeister (2005) is due to the assumption that relatively absorbing bands contribute nothing to k_{rad}, and that the opacity required to contribute to heat transport decreases with grain size.

6.3. Upper Mantle k_{rad}

Figure 7 shows predictions of k_{rad} in a typical upper mantle assemblage using our effective medium theory with phase fractions of 0.55/0.15/0.11/0.19 for olivine/orthopyroxene/clinopyroxene/garnet (similar to that shown in Figure 1). The colored lines show the grain size range of 0.01 to 10 cm, although grain sizes between 1 μm and 1 m are shown as black lines. The same predictions are also shown in Figure 7b as a function of grain size instead of temperature. Solid lines include all grain-size effects whereas dashed lines ignore scattering. The range 0.01 to 10 cm is highlighted as we presume it to be a reasonable bounds for most of the upper mantle. For this grain-size range, our model indicates that k_{rad} is always important, but that the range of variation at constant temperature is about a factor of two. Even in shear zones, which are thought to have grain sizes on the order of 50 μm or less (Precigout et al., 2017), k_{rad} remains more than negligible (Figure 7a). Notice that the significant dependence of k_{rad} on grain size continues over a more than five orders of magnitude range of grain size. The variation is also much larger overall than seen in single-phase polycrystals (Figure 6). The main reason for the large grain-size dependence in multiphase materials is the effective opacity mixing law. However, there is also a contribution from a large scattering interaction coefficient because interphase boundaries are stronger scatterers than same-phase grain boundaries.

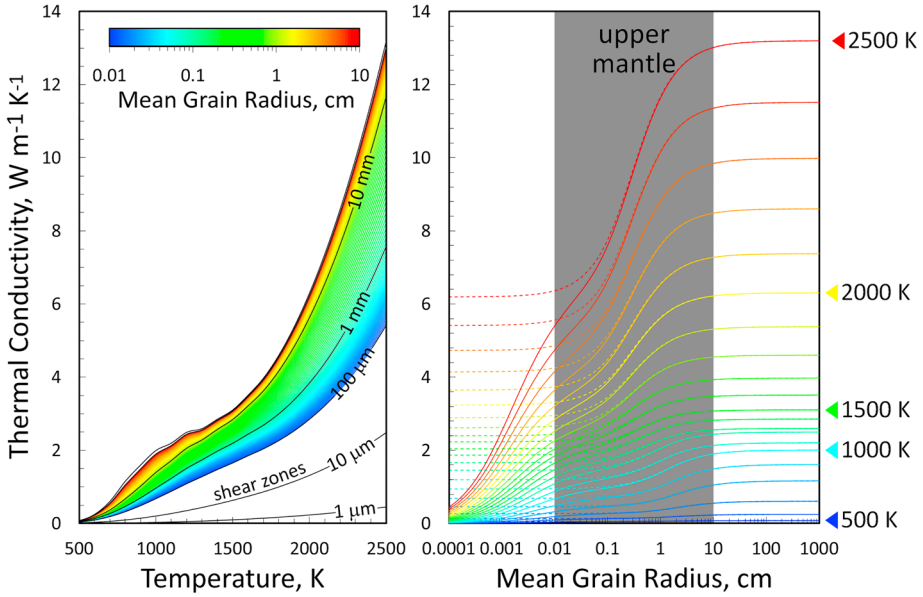

Figure 7. k_{rad} of an isotropic upper mantle assemblage predicted by our effective medium theory as a function of temperature and grain size.

6.4. Total Mantle Conductivity

To represent the lattice thermal conductivity of an upper mantle assemblage we use temperature dependent estimates for olivine, enstatite, augite, and garnet from Hofmeister et al. (2014, Table 3 therein). If we also include the effect of thermal resistance at grain boundaries (Smith et al., 2003) and pressure, the total thermal conductivity may be given as

$$k_{e,sum} = \left(\frac{1}{p} \prod_{k}^{N_k} \frac{1}{k_k^{\phi_k}} + \frac{R}{2r_m} \right)^{-1} + k_{rad}, \tag{26}$$

where $R = 10^{-8}$ m^2·K^{-1}·W^{-1} is grain boundary resistance per unit area and p is a parameter controlling pressure dependence (discussed later). Figure 8a shows $k_{e,sum}$ as a function of grain size and temperature calculated with our effective medium theory and no pressure effect ($p = 1$). k_{rad} in this result is the same as shown in Figure 7. High $k_{e,sum}$ values occur at low temperature due to the long mean-free

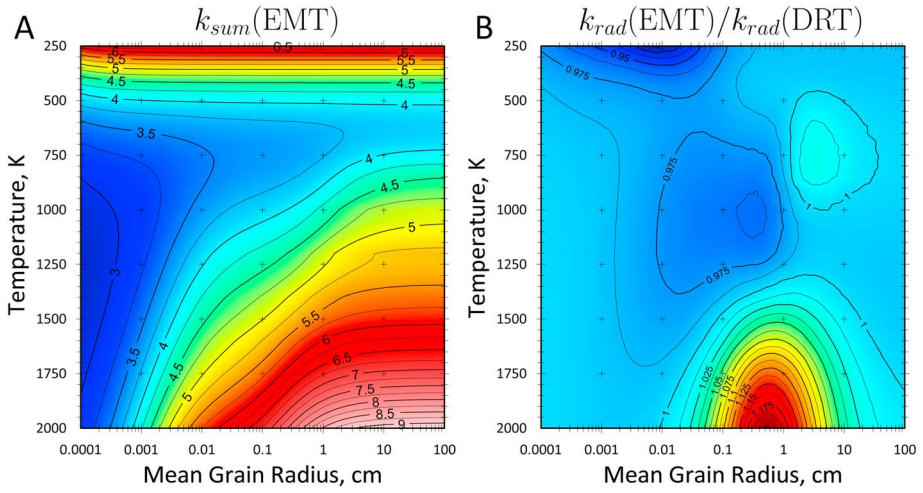

Figure 8. (a) k_{sum} (W·m^{-1}·K^{-1}) calculated by our effective medium theory (EMT) for an isotropic fertile peridotite assemblage as a function of temperature and grain size at zero pressure. (b) The ratio of k_{rad} predicted by our effective medium theory over Diffusive Radiation Transport (DRT) models. In these figures, isolines and the colorscale are consistent and represent the same data.

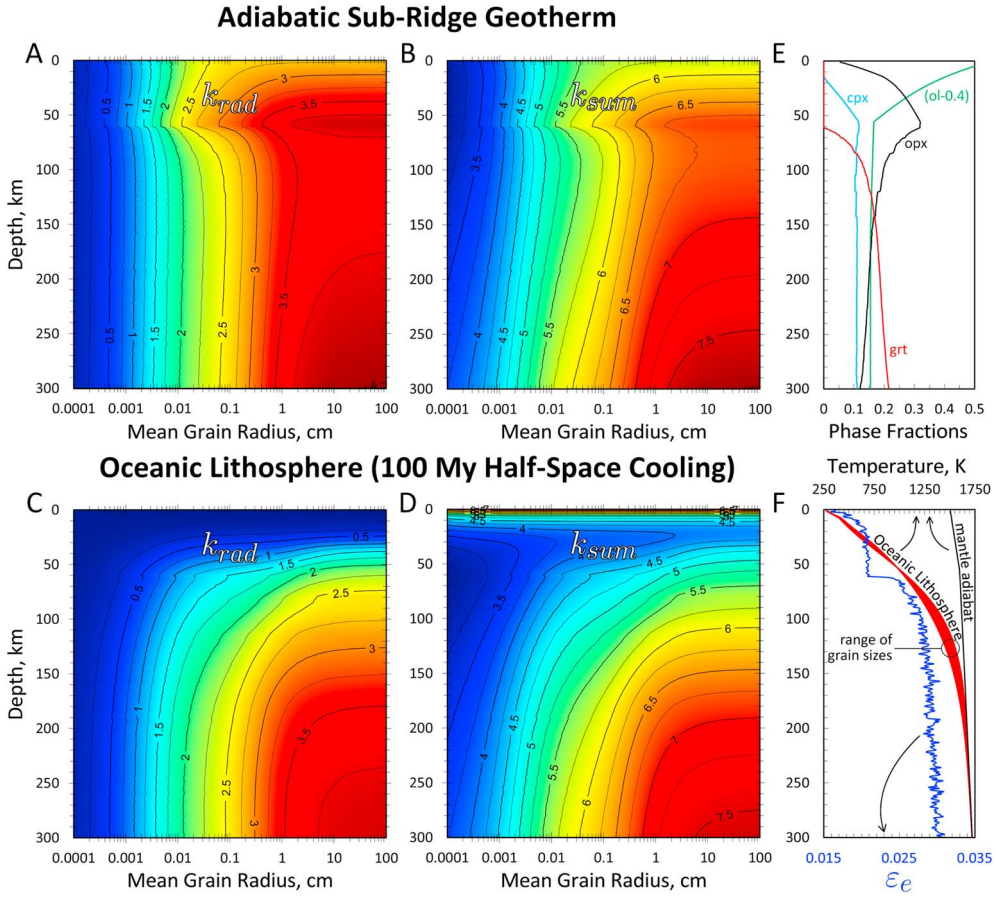

Figure 9. (a) Effective medium theory calculations of k_{rad} ($W{\cdot}m^{-1}{\cdot}K^{-1}$) as a function of depth and grain size in an upper mantle column beneath an ocean ridge consistent with phase fractions from thermodynamic calculations and contact statistics from isotropic equilibrium microstructures. (b) Same as in panel (a), except that k_{lat} as a function of temperature, pressure, and grain size is added to give k_{sum}. (c) Same as panel (a), except that the geotherm represents a 100 My old oceanic lithosphere. (d) Same as (b), except that the geotherm represents a 100 My old oceanic lithosphere. (e) Phase equilibrium predictions of phase fractions in the residue of melting (if melting occurs) from equilibrium thermodynamics and a melting model. (f) Geotherms for ridge oceanic column (black line) and oceanic lithosphere (red lines), models. Also shown is the scattering interaction coefficient ϵ_e as the blue line (see lower axis for values). In panels (a) to (d), isolines and the colorscale are consistent and represent the same data. cpx = clinopyroxene; ol = olivine; opx = orthopyroxene; grt = garnet.

path of phonons and at high temperature due to thermal radiation, with a minimum of 3.5 $W{\cdot}m^{-1}{\cdot}K^{-1}$ occurring around 750 K for reasonable mantle grain sizes. At high temperatures, such as those expected in thermal plumes (≈2000 K), $k_{e,sum}$ can reach more than 9 $W{\cdot}m^{-1}{\cdot}K^{-1}$. Figure 8b shows the ratio between k_{rad} calculated with our effective medium theory and Diffusive Radiation Transport estimates, showing that there is substantial agreement except at high temperatures around ~1 cm grain size. As remarked earlier, this is attributed to the fact that our Diffusive Radiation Transport calculations use synthetic microstructures which do not exactly represent random mixtures. The errors are most evident at high temperature because spectral bands where this effect is seen occur at high wave numbers (Figure S3) which only become important as thermal radiation is emitted at those wave numbers (Figure 5).

7. Geodynamic Applications

As example applications of our effective medium theory, we show thermal conductivity calculations for oceanic upper mantle. Figure 9a shows k_{rad} as a function of depth and grain size for the adiabatic mantle geotherm shown in Figure 9f. The potential temperature is 1573 K. The petrology of the upper mantle has been calculated following Grose and Afonso (2019). We use Gibbs free energy minimization using the software of Connolly (2009), the thermodynamic database of Xu et al. (2008), and the composition of the

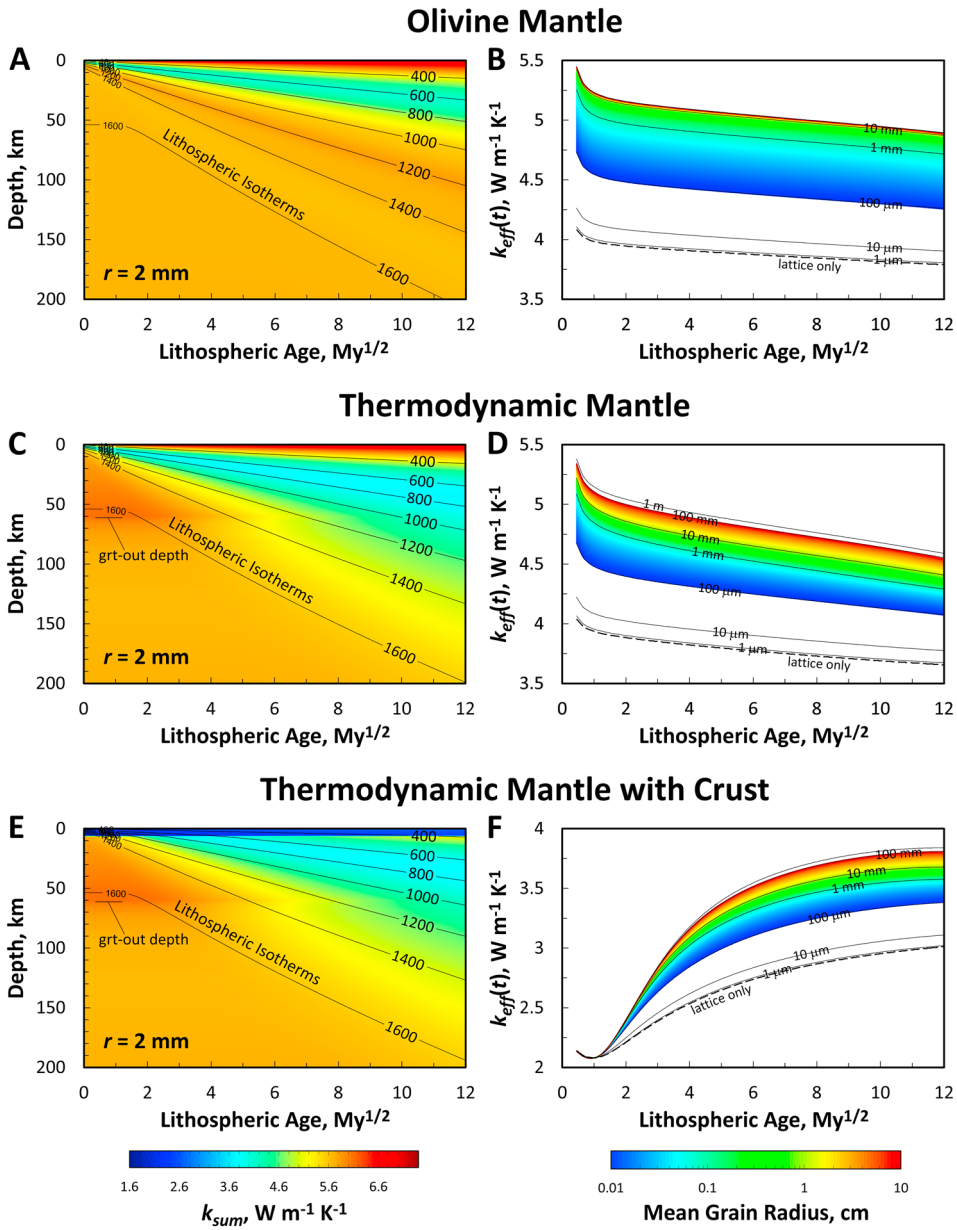

Figure 10. Illustration of three model results for the cooling of oceanic lithosphere. The left panels show isotherms (in Kelvin) overlying a map of total thermal conductivity k_{sum} of oceanic upper mantle (for the case of 2 mm grain size) as a function of depth and cooling age ($My^{1/2}$). The right panels show calculations of the effective thermal conductivity of the cooling mantle as a function of age. The top panels (a and b) show the case of a pure olivine polycrystalline mantle, middle panels (c and d) show the case of a thermodynamically consistent mantle petrology, and the bottom panels (e and f) show the case of a thermodynamic petrology with a 7-km insulating oceanic crust. Note that the crust is assumed to have $k_{rad} = 0$ in this numerical experiment.

residue for decompression melting of fertile peridotite from Herzberg (2004). Phase fractions are shown in Figure 9e and the scattering interaction coefficient ε_e has been calculated using unique 2-D microstructures calculated at each 1 km depth interval (Figure 9f). k_{sum} (equation (26)) for the same depth and grain size range is shown in Figure 9b with pressure dependence of k_{lat} described by (Hofmeister, 2007)

$$p = \frac{k_{e,lat}(P,T)}{k_{e,lat}(P_0,T)} = \exp\left(\frac{P}{K_T}\frac{\partial K_T}{\partial P}\right), \tag{27}$$

where P is pressure, P_0 is standard pressure, and we assume that $K_T = 135 + P\partial K_T/\partial P$ GPa is the bulk modulus and $\partial K_T/\partial P = 5.1$ is its pressure derivative. A phase-specific formulation would be more precise but

we do not address pressure-dependence in detail here. Figure S4 shows the arithmetic and harmonic means of the absorption coefficient as a function of depth and wave number. Figures 9c and 9d show analogous results for a 100 My oceanic lithosphere with the same petrology as before. Because lithospheric cooling depends on k and k depends on grain size, there is a range of geotherms for 100 My lithosphere as shown in Figure 9f.

An additional experiment we perform is a calculation of the effective thermal conductivity of the oceanic lithosphere as a function of age for three different case models. The calculation method is explained in supporting information section S8. The first case is that of a pure olivine mantle with results shown in Figures 10a and 10b. Figure 10a illustrates k_{sum} (case where $r_m = 2$ mm) of the upper mantle as a function of depth and lithospheric age with isotherms overlain, and Figure10b shows the effective thermal conductivity of the lithoshere k_{eff} as a function of age for a range of grain sizes. k_{eff} depends weakly on age because of a small dependence of k_{lat} on depth via the pressure (equation (27)) and adiabatic gradient. Also shown in Figures 10c–10f are analogous results for the case of a thermodynamically consistent petrology (as was shown in Figure 9e), and a thermodynamic petrology with an insulating oceanic crust. For the model with oceanic crust, k_{eff} is controlled by the low conductivity of the crust when the lithosphere is thin and young and becomes more influenced by the high conductivity of the mantle as the lithosphere thickens (Grose & Afonso, 2013, 2015). An important insight provided by these experiments is that although our k_{rad} model predicts substantially higher $k_{e,sum}$ at high temperature, the effect on the average behavior of the lithosphere is not far out of bounds from conventional geophysical theories. The total increase in mantle cooling from conductive transport through the lithosphere is on the order of 25% compared to lattice-only models.

7.1. Cautions and Caveats to Geodynamic Application

Our mantle k_{rad} estimates are generally similar to previous estimates for olivine polycrystals, although our values are significantly higher at ambient mantle temperature and large grain size (Figure 6). On the other hand, our values are much higher at all temperatures than more recent models (e.g., Hofmeister, 1999, 2005, 2014). Therefore, it may be necessary to reappraise the character of heat transport in a number of important geodynamic settings. However, some cautions are in order. First, our estimates depend on an incomplete spectral database. Future experimental studies must be performed to obtain better constraints on the spectra of upper mantle minerals at high temperature, in particular for pyroxenes and garnet. We have also not considered the role of the optical anisotropy of minerals or fabrics on the k_{rad} tensor. Our models are only reliable for isotropic equilibrium assemblages. This may be important to appreciate in applications to lithospheric geotherms since coherent large-scale lattice preferred orientations will induce geodynamically pertinent conductivity anisotropy. Although a detailed analysis is beyond the scope of the present work, we note that k_{rad} anisotropy is not in line with k_{lat} anisotropy. For example, in olivine, $k_{lat}^{[100]} > k_{lat}^{[001]} > k_{lat}^{[010]}$ (Pertermann & Hofmeister, 2006; Tommasi et al., 2001), but $A^{[100]} > A^{[001]} \approx A^{[010]}$ (Taran and Langer, 2001) which implies $k_{rad}^{[100]} < k_{rad}^{[001]} \approx k_{rad}^{[010]}$. Thus, it is expected that k_{rad} will partially counter k_{lat} anisotropy. We should also emphasize that we only considered uppermost mantle minerals. We have not considered high pressure polymorphs of olivine and pyroxene, or majorite. Data for transition zone minerals show that they are opaque (e.g., Thomas et al., 2012), suggesting low k_{rad}. Also, although the spectra of lower mantle minerals are controversial in detail, measurements so far accumulated indicate that they are exceptionally opaque (e.g., Goncharov et al., 2006, 2008, 2015; Keppler et al., 2008; Lobanov et al., 2016, 2017). Our models may thus be used to clarify details of opaque assemblages, but we do not contradict prior studies indicating that k_{rad} is low in these settings.

7.2. Suggestions for Routine k_{rad} Application

We have offered a mathematical description of k_{rad} which has some complexity, but a simple analytic form can be applied to geodynamic problems. The scattering effect is the most complicated because it requires knowledge of interphase contact statistics. Scattering could be ignored for large grain sizes. However, as we found that it varies little in the upper mantle (Figure 9f), it can be modeled well with $\varepsilon_{e,v}$ as a constant, or range of constants, between 0.015 and 0.03 for dunite and fertile mantle, respectively. The other parameters are easily calculated by mixing models if phase fractions and absorption spectra are known. To facilitate broader implementation, we provide a MATLAB code which calculates k_{rad} using our effective medium theory and the approximations of absorption spectra used here.

Data Statement

As this is a modeling study we do not report new data. Quantitative information consists of model results which are illustrated in the figures and discussed in the text. Modeling details are described in the supporting information. A MATLAB code for calculating k_{rad} using our effective medium theory is also available in the supporting information.

Acknowledgments
Thanks to Alexander Goncharov and Hans Keppler for helpful comments regarding their experimental results, and to John Howell for insightful comments regarding the n^2 factor in the radiation source function. George Rossman also provided insight on the available spectral data and values in the far infrared. Thanks to two reviewers for critical comments. The work of J. C. Afonso has been supported by two Australian Research Council Discovery Grants (DP120102372 and DP110104145). J. C. Afonso also acknowledges support from the Research Council of Norway through its Centers of Excellence funding scheme, Project 223272. C. J. Grose acknowledges support from NSF (grant 1826310). This is contribution 1341 from the Australian Research Council Centre of Excellence for Core to Crust Fluid Systems (http://www.ccfs.mq.edu.au) and 1308 in the GEMOC Key Centre (http://www.gemoc.mq.edu.au).

References

Abdulagatova, Z., Abdulagatov, I. M., & Emirov, V. N. (2009). Effect of temperature and pressure on the thermal conductivity of sandstone. *International Journal of Rock Mechanics and Mining Sciences*, *46*, 1055–1071.

Aronson, J. R., Bellotti, L. H., Eckroad, S. W., Emslie, A. G., McConnell, R. K., & von Thuna, P. C. (1970). Infrared spectra and radiative thermal conductivity of minerals at high temperatures. *Journal of Geophysical Research*, *75*, 3443–3456.

Clark, S. P. (1957). Absorption spectra of some silicates in the visible and near infrared. *American Mineralogist*, *43*, 732–742.

Clouet, J.-F. (1997). The Rosseland approximation for radiative transfer problems in heterogeneous media. *Journal of Quantitative Spectroscopy & Radiative Transfer*, *58*(1), 33–43.

Connolly, J. A. D. (2009). The geodynamic equation of state: What and how. *Geochemistry, Geophysics, Geosystems*, *10*, Q10014. https://doi.org/10.1029/2009GC002540

Deer, W. A., Howie, R. A., & Zussman, J. (1997). *Rock-forming minerals: Single-chain silicates* (Vol. 2A, pp. 668). London: Geological Society of London.

Denlinger, R. P. (1992). A revised estimate for the temperature structure of the oceanic lithosphere. *Journal of Geophysical Research*, *97*, 7219–7222.

Dubuffet, F., Yuen, D. A., & Rainey, E. S. G. (2002). Controlling thermal chaos in the mantle by positive feedback from radiative thermal conductivity. *Nonlinear Processes in Geophysics*, *9*, 311–323.

Fuchs, S., Schutz, F., Forster, H.-J., & Forster, A. (2013). Evaluation of common mixing models for calculating bulk thermal conductivity of sedimentary rocks: Correction charts and new conversion equations. *Geothermics*, *47*, 40–52.

Fukao, Y., Mizutani, H., & Uyeda, S. (1968). Optical absorption spectra at high temperatures and radiative thermal conductivity of olivines. *Physics of the Earth and Planetary Interiors*, *1*, 57–62.

Goncharov, A. F., Beck, P., Struzhkin, V. V., Haugen, B. D., & Jacobsen, S. D. (2009). Thermal conductivity of lower-mantle minerals. *Physics of the Earth and Planetary Interiors*, *174*, 23–32.

Goncharov, A. F., Haugen, B. D., Struzhkin, V. V., Beck, P., & Jacobsen, S. D. (2008). Radiative conductivity in the Earth's lower mantle. *Nature*, *456*, 231–234.

Goncharov, A. F., Lobanov, S. S., Tan, X., Hohensee, G. T., Cahill, D. G., Lin, J.-F., et al. (2015). Experimental study of thermal conductivity at high pressures: Implications for the deep Earth's. *Physics of the Earth and Planetary Interiors*, *247*, 11–16.

Goncharov, A. F., Struzhkin, V. V., & Jacobsen, S. D. (2006). Reduced radiative conductivity of low-spin (Mg,Fe)O in the lower mantle. *Science*, *312*, 1205–1208.

Grose, C. J., & Afonso, J. C. (2013). Comprehensive plate models for the thermal evolution of oceanic lithosphere. *Geochemistry, Geophysics, Geosystems*, *14*, 3751–3778. https://doi.org/10.1002/ggge.20232

Grose, C. J., & Afonso, J. C. (2015). The hydrothermal power of oceanic lithosphere. *Solid Earth*, *6*, 1131–1155.

Grose, C. J., & Afonso, J. C. (2019). Chemical disequilibria, lithospheric thickness, and the source of ocean island basalts. *Journal of Petrology*, egz012. https://doi.org/10.1093/petrology/egz012

Hasterok, D. (2013). A heat flow based cooling model for tectonic plates. *Earth and Planetary Science Letters*, *311*, 386–395.

Hasterok, D., & Chapman, D. S. (2007). Continental thermal isostasy: 1. Methods and sensitivity. *Journal of Geophysical Research*, *112*, B06414. https://doi.org/10.1029/2006JB004663

Hasterok, D., & Chapman, D. S. (2011). Heat production and geotherms for continental lithosphere. *Earth and Planetary Science Letters*, *307*, 59–70.

Herzberg, C. (2004). Geodynamic information in peridotite petrology. *Journal of Petrology*, *45*(12), 2507–2530.

Hofmeister, A. M. (1999). Mantle values of thermal conductivity and the geotherm from phonon lifetimes. *Science*, *283*, 1699.

Hofmeister, A. M. (2005). Dependence of diffusive radiative transfer on grain-size, temperature, and Fe-content: Implications for mantle processes. *Journal of Geodynamics*, *40*, 51–72.

Hofmeister, A. M. (2007). Pressure dependence of thermal transport properties. *Proceedings of theNational Academy of Sciences*, *104* (22), 9192–9197. https://doi.org/10.1073/pnas.0610734104

Hofmeister, A. M. (2014). Thermodynamic and optical thickness corrections to diffusive radiative transfer formulations with application to planetary interiors. *Geophysical Research Letters*, *41*, 3074–3080. https://doi.org/10.1002/2014GL059833

Hofmeister, A. M., Dong, J., & Branlund, J. M. (2014). Thermal diffusivity of electrical insulators at high temperatures: Evidence for diffusion of bulk phonon-polaritons at infrared frequencies augmenting phonon heat conduction. *Journal of Applied Physics*, *115*(163517). https://doi.org/10.1063/1.4873295

Hofmeister, A. M., & Yuen, D. A. (2007). Critical phenomena in thermal conductivity: Implications for lower mantle dynamics. *Journal of Geodynamics*, *44*, 186–199.

Howell, J. R., Siegel, R., & Menguc, M. P. (2011). *Thermal radiation heat transfer* (5th ed.), (pp. 987). Boca Raton, FL: CRC Press.

Janssens, K. G. F., Raabe, D., Kozeschnik, E., Miodownik, M. A., & Nestler, B. (2007). *Computational materials engineering: An introduction to microstructure evolution*. London, UK: Elsevier Academic Press.

Keppler, H., Dubrovinsky, L. S., Narygina, O., & Kantor, I. (2008). Optical absorption and radiative thermal conductivity of silicate perovskite to 125 Gigapascals. *Science*, *322*, 1529–1532.

Laskowski, T. E., & Scotford, D. M. (1980). Rapid determination of olivine compositions in thin section using dispersion staining methodology. *American Mineralogist*, *65*, 401–403.

Lay, T., Hernlund, J., & Buffett, B. A. (2008). Core-mantle boundary heat flow. *Nature Geoscience*, *1*, 25–32.

Lobanov, S. S., Holtgrewe, N., & Goncharov, A. F. (2016). Reduced radiative conductivity of low spin FeO_6-octahedra in $FeCO_3$ at high pressure and temperature. *Earth and Planetary Science Letters*, *449*, 20–25.

Lobanov, S. S., Holtgrewe, N., Lin, J.-F., & Goncharov, A. F. (2017). Radiative conductivity and abundance of post-perovskite in the lowermost mantle. *Earth and Planetary Science Letters*, *479*, 43–49.

Maierova, P., Chust, T., Steinle-Neumann, G., Cadek, O., & Cizkova, H. (2012). The effect of variable thermal diffusivity on kinematic models of subduction. *Journal of Geophysical Research*, *117*, B07202. https://doi.org/10.1029/2011JB009119

Matyska, C., & Yuen, D. A. (2007). Lower-mantle material properties and convection models of multiscale plumes. *Geological Society of America Special Paper*, *430*, 137–163.

Nitsan, U. (1976). Effect of scattering on radiative heat transfer in the Earth's mantle. *Eos Transactions American Geophysical Union*, *57*, 12.

Parsons, B., & Sclater, J. G. (1977). An analysis of the variation of ocean floor bathymetry and heat flow with age. *Journal of Geophysical Research*, *82*, 803–827.

Pertermann, M., & Hofmeister, A. M. (2006). Thermal diffusivity of olivine-group minerals at high temperature. *American Mineralogist*, *91*, 1747–1760.

Pitt, G. D., & Tozer, D. C. (1970). Radiative heat transfer in dense media and its magnitude in olivines and some other ferromagnesian minerals under typical upper mantle conditions. *Physics of the Earth and Planetary Interiors*, *2*, 189–199.

Pomraning, G. C. (1988). Radiative transfer in random media with scattering. *Journal of Quantitative Spectroscopy & Radiative Transfer*, *40*(4), 479–487.

Precigout, J., Prigent, C., Palasse, L., & Pochon, A. (2017). Water pumping in 545 mantle shear zones. *Nature Communications*, *8*, 15736. https://doi.org/10.1038/ncomms15736

Rosseland, S. (1936). *Theoretical astrophysics: Atomic theory and the analysis of stellar atmospheres and envelopes*. Oxford: Clarendon Press.

Schatz, J. F., & Simmons, G. (1972). Thermal conductivity of Earth materials at high temperatures. *Journal of Geophysical Research*, *77*, 6966–6983.

Sclater, J. G., & Francheteau, J. (1970). The implications of terrestrial heat flow observations on current tectonic and geochemical models of the crust and upper mantle of the Earth. *Geophysical Journal International*, *20*, 509–542.

Stevenson, D. J. (2003). Planetary magnetic fields. *Earth and Planetary Science Letters*, *208*, 1–11.

Shankland, T. J., Nitsan, U., & Duba, A. G. (1979). Optical absorption and radiative heat transport in olivine at high temperature. *Journal of Geophysical Research*, *84*, 1603–1610.

Shärmeli (1979). Identification of radiative thermal conductivity of olivine up to 25 kbar and 1500 K, *High-pressure science and technology, sixth AIRAPT conference* (Vol. 2, pp. 60–74). New York: Plenum.

Sleep, N. S. (2011). Small-scale convection beneath oceans and continents. *Chinese Science Bulletin*, *56*, 1292–1317.

Smith, D. S., Fayette, S., Grandjean, S., & Martin, C. (2003). Thermal resistance of grain boundaries in alumina ceramics and refractories. *Journal of the American Ceramic Society*, *86*(1), 105–111.

Sriramadas (1957). Diagrams for the correlation of unit cell edges and refractive indices with the chemical composition of garnets. *American Mineralogist*, *42*, 293–298.

Syracuse, E. M., vanKeken, P. E., & Abers, G. A. (2010). The global range of subduction zone thermal models. *Physics of the Earth and Planetary Interiors*, *183*(1-2), 73–90.

Taran, M. N., Dyar, M. D., & Matsyuk, S. S. (2007). Optical absorption study of natural garnets of almandine-skiagite composition showing intervalence $Fe^{2+}+Fe^{3+} \rightarrow Fe^{3+}+Fe^{2+}$ charge-transfer transition. *American Mineralogist*, *92*, 753–760.

Taran, M. N., & Langer, K. (2001). Electronic absorption spectra of Fe2+ ions in oxygen-based rock-forming minerals at temperatures between 297 and 600 K. *Physics and Chemistry of Minerals*, *28*, 199–210.

Thomas, S. M., Bina, C. R., Jacobsen, S. D., & Goncharov, A. F. (2012). Radiative heat transfer in a hydrous mantle transition zone. *Earth and Planetary Science Letters*, *357-358*, 130–136.

Tikare, V., Holm, E. A., Fan, D., & Chen, L. Q. (1998). Comparison of phase-field and Potts models for coarsening processes. *Acta Materialia*, *47*, 363–371.

Tommasi, A., Gibert, B., Seipold, U., & Mainprice, D. (2001). Anisotropy of thermal diffusivity in the upper mantle. *Nature*, *411*, 783–786.

Ullrich, K., Langer, K., & Becker, K. D. (2002). Temperature dependence of the polarized electronic absorption spectra of olivines. Part 1—Fayalite. *Physics and Chemistry of Minerals*, *29*, 409–419. https://doi.org/10.1007/s00269-002-0248-4

van den Berg, A. P., Rainey, E. S. G., & Yuen, D. A. (2005). The combined influences of variable thermal conductivity, temperature- and pressure-dependent viscosity and core-mantle coupling on thermal evolution. *Physics of the Earth and Planetary Interiors*, *149*, 259–278.

Vanderhaegen, D. (1988). Impact of a mixing structure on radiative transfer in random media. *Journal of Quantitative Spectroscopy & Radiative Transfer*, *39*(4), 333–337.

Xu, W., Lithgow-Bertelloni, C., Stixrude, L., & Ritsema, J. (2008). The effect of bulk composition and temperature on mantle seismic structure. *Earth and Planetary Science Letters*, *275*, 70–79.

Zlotnik, S., Afonso, J. C., Diez, P., & Fernandez, M. (2008). Small-scale gravitational instabilities under the oceans: Implications for the evolution of oceanic lithosphere and its expression in geophysical observables. *Philosophical Magazine*, *88*(28), 3197–3217.

References from Supporting Information

Gerya, T. V., & Yuen, D. A. (2003). Characteristics-based marker-in-cell method with conservative finite-differences schemes for modeling geological flows with strongly variable transport properties. *Physics of the Earth and Planetary Interiors*, *140*, 293–318.

Klemens, P. G., & Greenberg, I. N. (1973). Radiative heat transfer through composite materials. *Journal of Applied Physics*, *44*, 2992. https://doi.org/10.1063/1.1662694

Majaron, B., Milanic, M., & Premru, J. (2015). Monte Carlo simulation of radiation transport in human skin with rigorous treatment of curved tissue boundaries. *Biomedical Optics*, *20*(1), 015002.

Planck, M. (1914). The theory of heat radiation, translated by Morton Masius (June 18, 2012).

Pomraning, G. C. (1989). Statistics, renewal theory, and particle transport. *Journal of Quantitative Spectroscopy & Radiative Transfer*, *42*(4), 279–293.

Porter, D., & Easterling, K. (1981). *Phase transformations in metals and alloys*. New York: Van Nostrand Reinhold Co. Ltd.

Rybicki, G. B., & Lightman, A. P. (2004). *Radiative processes in astrophysics*. Weinheim: Wiley-Vch Verlag GmbH & Co KGaA.

Seaid, M. (2007). Multigrid Newton-Krylov method for radiation in diffusive semitransparent media. *Journal of Computational and Applied Mathematics*, *203*, 498–515.

Sharkov, E. A. (2003). *Passive microwave remote sensing of the Earth*, pp. 613. Verlag Berlin Heidelberg: Springer.

Viskanta, R., & Anderson, E. E. (1975). Heat transfer in semitransparent solids. *Advances in Heat Transfer*, *11*, 317–441.

Xia, Xin-Lin, Huang, Y., Tan, H.-P., & Zhang, X.-B (2002). Simultaneous radiation and conduction heat transfer in a graded index semitransparent slab with gray boundaries. *International Journal of Heat and Mass Transfer*, *45*, 2673–2688.